Supporting Information

Baron and Vellore 10.1073/pnas.1207892109

SI Text

SI Methodological Details. A first MD simulation of unbound LSD1/CoREST was initialized from the X-ray structure by Yang et al. (1, 2) (PDB ID code 2IW5; 0.26-nm resolution). A second MD simulation of LSD1/CoREST bound to the H3-histone N-terminal tail (16 residues) was initialized from the X-ray structure by Forneris et al. (3) (PDB ID code 2V1D; 0.31-nm resolution). In both cases, conformational dynamics in solution was investigated for the LSD1-CoREST complex noncovalently bound to $FADH^-$. These X-ray structures provided initial coordinates for the atoms of the protein, the cofactor (and the substrate), while crystallographic water sites were taken from PDB ID code 2IW5 (4) in both cases (water sites overlapping with the H3-pepitde were removed in the H3-bound simulation). The initial configurations were solvated under rectangular periodic boundary conditions in a (pre-equilibrated) water box large enough to avoid interactions between mirror images along the entire MD trajectory. The final unbound system was neutralized with 2 Cl^- ions and contained 60,106 water molecules. The final H3-bound system contained 6 Cl^- ions, 1 Na^+ ion, and 60,093 water molecules. The MD trajectory was generated and analyzed in double precision using the GROMACS 4.5.4 software (5). Force field parameters and charges were set from the parameter set 53A6 (6) of the GROMOS force field to reproduce the experimental condition of apparent neutral pH. GROMOS-compatible SPC water model (7) and ion parameters (8) were employed. To avoid the distortion of the planar $FADH^-$ rings, in agreement with recent studies (9, 10), improper dihedral parameters for the flavin rings (i.e. excluding those for bound hydrogen atoms and carbonyls and methyl groups) were attributed parameters as for the heme group (i.e. force constant of 0.204 instead of 0.051 kJ mol^{-1} deg^{-2}).

A first steepest-descent energy minimization was performed in order to relax the initial solvent and ion configuration, while the position of protein atoms and of the crystallographic-water oxygen atoms were restrained using a harmonic potential (force constant of 2,000 kJ mol^{-1} nm^{-2}). Next, a steepest-descent energy minimization was performed with no restraints to eliminate any residual strain. The energy minimization runs ended whenever the energy change per step became <0.5 kJ mol^{-1}. MD simulations were initialized from the energy-minimized configurations with atomic velocities taken from Maxwell–Boltzmann distributions at 50 K, while the position of protein atoms were restrained using a harmonic potential (force constant of 2,000 kJ mol^{-1} nm^{-2}). Each system was then gradually brought to the reference temperature of 300 K in 11 consecutive 250-ps periods of simulations. During each period the reference temperature was incremented by 25 K and the force constant decreased by 250 kJ mol^{-1} nm^{-2}. An initial equilibration period was performed for each system and extended for 5 ns to equilibrate the energy components and the system pressure.

Newton's equations of motion were integrated using the leap-frog algorithm (11) with a 2-fs time step. The P-LINCS numerical algorithm (12) was applied to constrain all bond lengths (fourth order expansion), excluding water molecules which were kept rigid using the SETTLE analytical algorithm (13). All simulations were carried out in the N, p, T ensemble by separately coupling the temperature of LSD1, COREST, $FADH^-$, and solvent degrees of freedom to a heat bath. During the heat-up phase only the system temperature was weakly coupled (relaxation time 0.1 ps) to a heat bath (14) and the pressure (estimated based on an atomic virial) to a pressure bath (14) via isotropic coordinate scaling (relaxation time 0.5 ps; isothermal compressibility 4.574 10^{-4} $[\text{kJ mol}^{-1}\,\text{nm}^{-3}]^{-1}$). During the production runs, canonical ensembles were obtained using the Nosé–Hoover extended-ensemble thermostat (15, 16) to maintain the temperature (300 K) and the Parrinello–Rahman extended-ensemble barostat (17) (relaxation time 5 ps; isothermal compressibility 4.574 10^{-4} $[\text{kJ mol}^{-1}\,\text{nm}^{-3}]^{-1}$) to maintain the system pressure (1 atm). The use of thermostat and barostat algorithms different between heat-up and equilibrium phases is well motivated considering that weak-coupling algorithms do not suffer from numerical divergences from the reference temperature and pressure values even when far away from such reference values. Weak-coupling does ensure N, p, T ensembles during the heat-up phase, although not canonical N, p, T ensembles, which we instead enforce during our MD runs once the system reached the desired temperature of 300 K and pressure of 1 atm. Full treatment of electrostatic interactions was achieved using a smooth particle mesh Ewald approximation (18) (grid dimension 0.12 nm; fourth order interpolation). Nonbonded interactions were shifted (see *appendix* in ref. 19) to zero at a distance of 1.4 nm, recalculated every time step in the range 0.0–0.8 nm and every five time steps in the range 0.8–1.4 nm, using a twin-range cutoff scheme (20).

Trajectory snapshots were extracted every 10 ps for analysis (i.e., 50,000 MD snapshots) and used for analysis in double precision using the GROMACS 4.5.4 (5). Whenever else specified, structural fitting was performed by (*i*) superimposing the centers of mass (to remove overall translation) and (*ii*) performing an atom-positional least-square fitting procedure (to remove overall rotation) using all C^α atoms (21). The occurrence of secondary structure elements was monitored according to the definition by Kabsch and Sander (22). We investigated the dominant protein motion connecting these clamp states by principal component analysis (PCA) of protein fluctuations (23, 24) with the bio3d software (25) and displayed using VMD (26) (see Movies S1–S6). PCA analysis was performed after superimposition of the MD trajectory snapshots on the C^α atoms of LSD1/CoREST Tower domain, which is essentially a rigid body during the entire MD period. The 2WI5 X-ray model was used for this superimposition for PCA of both the unbound and H3-bound ensembles. Calculation of the relative free energy maps was performed using standard approaches based on the probability distribution, after binning the actual simulation data (100×100 elements grid). Calculations of the H3-tail pocket volume were performed with POVME (27) by defining the pocket using residues in ranges Ala354–Tyr363, Val370–Tyr391, and Leu529–His564. In this case, only the C^α atoms of these residues were used for structural fitting prior to volume calculation and the structure PDB 2IW5 (4) was used for fitting from both simulations. We note that the qualitative volume trends reported are independent of alternative, similar definitions of the H3 pocket.

1. Yang M, et al. (2006) Structural basis for CoREST-dependent demethylation of nucleosomes by the human LSD1 histone demethylase. *Mol Cell* 23:377–387.
2. Stavropoulos P, Blobel G, Hoelz A (2006) Crystal structure and mechanism of human lysine-specific demethylase-1. *Nat Struct Mol Biol* 13:626–632.
3. Yang M, et al. (2007) Structural basis of histone demethylation by LSD1 revealed by suicide inactivation. *Nat Struct Mol Biol* 14:535–539.
4. Yang M, et al. (2006) Structural basis for CoREST-dependent demethylation of nucleosomes by the human LSD1 histone demethylase. *Mol Cell* 23:377–387.

5. Hess B, Kutzner C, van der Spoel D, Lindahl E. (2008) GROMACS 4: Algorithms for highly efficient, load-balanced, and scalable molecular simulation. *J Chem Theory Comput* 4:435–447.
6. Oostenbrink C, Villa A, Mark AE, van Gunsteren WF (2004) A biomolecular force field based on the free enthalpy of hydration and solvation: The GROMOS force-field parameter sets 53A5 and 53A6. *J Comput Chem* 25:1656–1676.
7. Berendsen HJC (1981) *Interaction Models for Water in Relation to Protein Hydration* (Pullman, B. E., Ordrecht), pp 331–342.
8. Åqvist J (1990) Ion water interaction potentials derived from free-energy perturbation simulations. *J Phys Chem* 94:8021–8024.
9. Bhattacharyya S, Stankovich MT, Truhlar DG, Gao J (2007) Combined quantum mechanical and molecular mechanical simulations of one- and two-electron reduction potentials of flavin cofactor in water, medium-chain acyl-CoA dehydrogenase, and cholesterol oxidase. *J Phys Chem A* 111:5729–5742.
10. Baron R, Binda C, Tortorici M, McCammon JA, Mattevi A (2011) Molecular mimicry and ligand recognition in binding and catalysis by the histone demethylase LSD1-CoREST complex. *Structure* 19:212–220.
11. Ryckaert JP, Ciccotti G, Berendsen HJC (1977) Numerical-integration of cartesian equations of motion of a system with constraints-molecular-dynamics of N-alkanes. *J Comput Phys* 23:327–341.
12. Hess B (2008) P-LINCS: A parallel linear constraint solver for molecular simulation. *J Chem Theory Comput* 4:116–122.
13. Miyamoto S, Kollman PA (1992) Settle—An analytical version of the shake and rattle algorithm for rigid water models. *J Comput Chem* 13:952–962.
14. Berendsen HJC, Postma JPM, van Gunsteren WF, DiNola A, Haak JR (1984) Molecular-dynamics with coupling to an external bath. *J Chem Phys* 81:3684–3690.
15. Hoover W (1989) Generalization of Nose's isothermal molecular-dynamics—non-Hamiltonian dynamics for the canonical ensemble. *Phys Rev A* 40:2814–2815.
16. Nosè S (1984) A unified formulation of the constant temperature molecular-dynamics methods. *J Chem Phys* 81:511–519.
17. Parrinello M, Rahman A (1981) Polymorphic transitions in single-crystals—A new molecular-dynamics method. *J App Phys* 52:7182–7190.
18. Essmann U, et al. (1995) A smooth particle mesh Ewald method. *J Chem Phys* 103:8577–8593.
19. Baron R, et al. (2007) Comparison of thermodynamic properties of coarse-grained and atomic-level simulation models. *ChemPhysChem* 8:452–461.
20. van Gunsteren WF, Berendsen HJC (1990) Computer-simulation of molecular-dynamics—Methodology, applications, and perspectives in chemistry. *Angew Chem Int Ed Engl* 29:992–1023.
21. McLachlan AD (1979) Gene duplications in the structural evolution of chymotrypsin. *J Mol Biol* 128:49–79.
22. Kabsch W, Sander C (1983) Dictionary of protein secondary structure—pattern-recognition of hydrogen-bonded and geometrical features. *Biopolymers* 22:2577–2637.
23. Garcia AE (1992) Large-amplitude nonlinear motions in proteins. *Phys Rev Lett* 68:2696–2699.
24. Amadei A, Linssen AB, Berendsen HJ (1993) Essential dynamics of proteins. *Proteins* 17:412–425.
25. Grant BJ, Rodrigues APC, ElSawy KM, McCammon JA, Caves LSD (2006) Bio3d: An R package for the comparative analysis of protein structures. *Bioinformatics* 22:2695–2696.
26. Humphrey W, Dalke A, Schulten K (1996) VMD: Visual molecular dynamics. *J Mol Graph* 14:33–38.
27. Durrant JD, de Oliveira CAF, McCammon JA (2011) POVME: An algorithm for measuring binding-pocket volumes. *J Mol Graph Mod* 29:773–776.

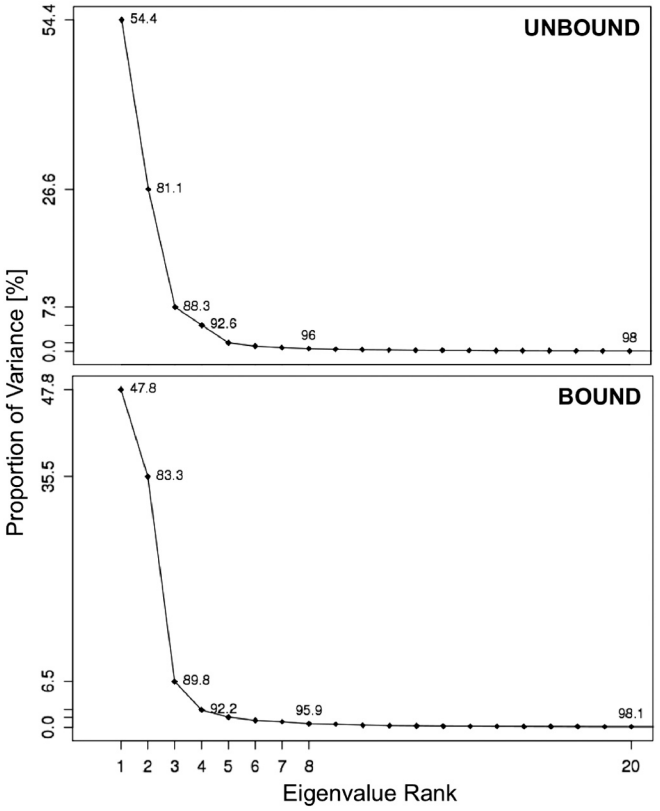

Fig. S1. Cumulative contribution of the principal components of LSD1/CoREST dynamics. (*Top*) Unbound state; (*Bottom*) H3-bound state. PC cumulative relative contributions are ordered by increasing eigenvalue frequencies. Note that PC1, PC2, and PC3 together capture 88.3% and 89.8% of the overall LSD1/CoREST C^{α}-atom fluctuation along the 0.5 μs MD trajectories, respectively.

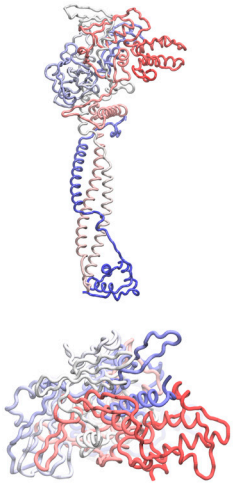

Movie S1. This movie shows the motion of the unbound LSD1/CoREST complex as captured by the most dominant backbone C^{α}-atom principal component, PC1. This motion involves a rigid-body rotation of the AOD domain with respect to the Tower domain. Lateral and top view representations are displayed maintaining identical relative orientation of the Tower domain.

Movie S1 (MOV)

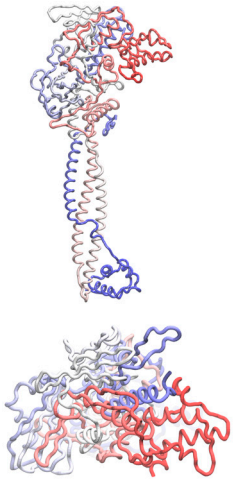

Movie S2. This movie shows the motion of the unbound LSD1/CoREST complex as captured by the second-most dominant backbone C^{α}-atom principal component, PC1. These fluctuations are responsible for the clamp-closed to clamp-open reversible oscillation between SWIRM and SAINT2 domains. Lateral and top view representations are displayed maintaining identical relative orientation of the Tower domain.

Movie S2 (MOV)

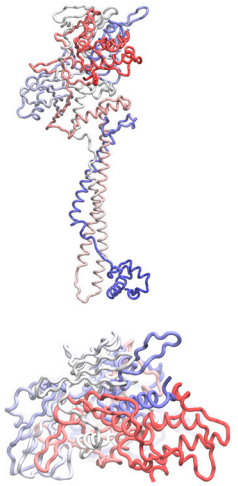

Movie S3. This movie shows the motion of the unbound LSD1/CoREST complex as captured by the third-most dominant backbone C^{α}-atom principal component, PC3. This motion is a rigid-body rotation of the AOD domain around an axis defined along the Tower domain. Lateral and *Top* view representations are displayed maintaining identical relative orientation of the Tower domain.

Movie S3 (MOV)

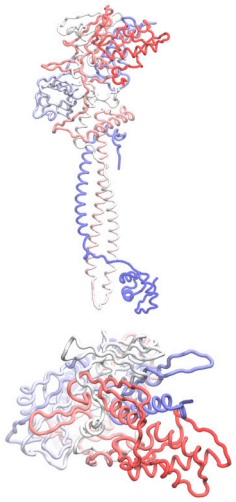

Movie S4. This movie shows the motion of the H3-bound LSD1/CoREST complex as captured by the most dominant backbone C^{α}-atom principal component, PC1. These fluctuations are responsible for the clamp-closed to clamp-open reversible oscillation between SWIRM and SAINT2 domains. Lateral and top view representations are displayed maintaining identical relative orientation of the Tower domain.

Movie S4 (MOV)

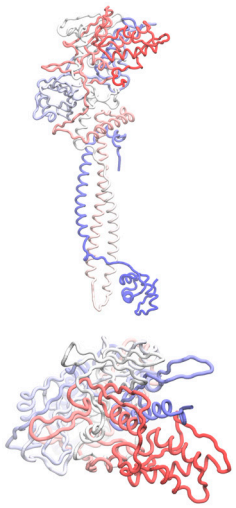

Movie S5. This movie shows the motion of the H3-bound LSD1/CoREST complex as captured by the second-most dominant backbone C^{α}-atom principal component, PC1. These fluctuations are responsible for a twist of the AOD domain with respect to the Tower domain. Lateral and top view representations are displayed maintaining identical relative orientation of the Tower domain.

Movie S5 (MOV)

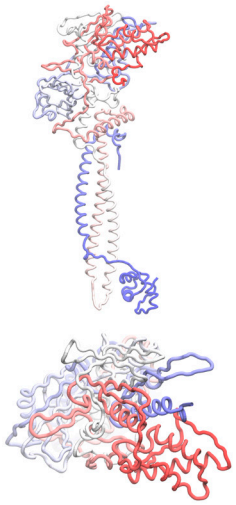

Movie S6. This movie shows the motion of the H3-bound LSD1/CoREST complex as captured by the third-most dominant backbone C^{α}-atom principal component, PC3. This motion is a rigid-body rotation of the AOD domain around an axis defined by the Tower domain. Lateral and top view representations are displayed maintaining identical relative orientation of the Tower domain.

Movie S6 (MOV)